THE JOURNAL OF PHYSICAL CHEMISTRY C

pubs.acs.org/JPCC Article

Incorporation of Europium in Bi_2Te_3 Topological Insulator Epitaxial Films

Celso I. Fornari,* Hendrik Bentmann, Sérgio L. Morelhão, Thiago R. F. Peixoto, Paulo H. O. Rappl, Abdul-Vakhab Tcakaev, Volodymyr Zabolotnyy, Martin Kamp, Tien-Lin Lee, Chul-Hee Min, Philipp Kagerer, Raphael C. Vidal, Anna Isaeva, Michael Ruck, Vladimir Hinkov, Friedrich Reinert, and Eduardo Abramof

Cite This: *J. Phys. Chem. C* 2020, 124, 16048−16057 Read Online

ACCESS | Metrics & More | Article Recommendations

ABSTRACT: In the field of topological materials, the interaction between band topology and magnetism remains a current frontier for the advancement of new topological states and spintronic functionalities. Doping with rare-earth elements with large magnetic moments is a current approach to exploit the phenomenology of such interaction. However, dopant solubility into the main matrix plays a major role. In this sense, the present work is focused on elucidating how Eu incorporates into Bi_2Te_3 lattice as a function of doping. This work reports a systematic investigation of the structural and electronic properties of bismuth telluride epitaxial layers doped with Eu. Bi_2Te_3 films were grown by molecular beam epitaxy on (111) BaF_2 substrates with nominal Eu doping ranging from 0% up to 9%. X-ray diffraction analysis and scanning transmission electron microscopy reveal that Eu atoms enter substitutionally on Bi sites up to 4% of Eu doping. In contrast, the 9% Eu-doped sample contains epitaxially oriented nanoclusters of EuTe. X-ray photoelectron and absorption spectroscopies show that Eu atoms enter the Bi_2Te_3 crystal matrix in the divalent Eu^{2+} state for all Eu concentrations. Angle-resolved photoemission experiments indicate that the topological surface state is preserved in the presence of the local magnetic moments introduced by the Eu impurities.

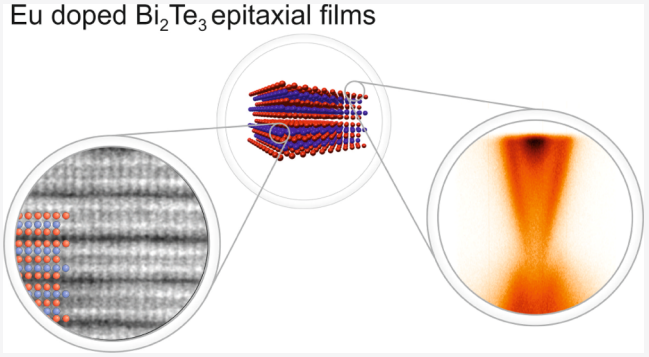

INTRODUCTION

The interplay of band topology and magnetism represents one of the central frontiers in the field of topological materials, and it is believed to provide various pathways for the realization of novel topological states of matter and spintronic functionalities. For instance, the quantum anomalous Hall effect has been realized in a topological insulator (TI) doped with magnetic impurities, namely, in V- and Cr-doped $(BiSb)_2Te_3$. In the past years, transition-metal-doped TIs have been widely studied.[1−9] More recently, intrinsic magnetic TI have been discovered,[10−13] which also display topological transport phenomena in thin films.[14,15] Despite these encouraging developments, the impact of local magnetic moments and magnetic order on topological surface states (TSS) is not yet fully understood.[10−13,16−18] For example, gap openings in the TSS have been observed even in the paramagnetic regime of some materials,[5,17] while in other cases, no gap was observed in the presence of magnetic order.[13]

Doping with rare-earth elements (RE) is an alternative approach to address the interplay of magnetism and TSS. REs typically feature a large and localized magnetic moment arising from the partially filled 4f shell. In the archetypal 3D TI[19] Bi_2Te_3, it is expected that RE elements would lead to an isoelectronic and substitutional doping on the Bi site, avoiding electrical doping.[20] Previously, Bi_2Te_3 has been doped with Dy, Ho, and Gd. Out of the three, Dy^{3+} and Ho^{3+} exhibit the highest calculated magnetic moment of around 10.5 μ_B, while for Gd^{3+}, this value is around 7.9 μ_B.[21]

A previously not investigated 4f dopant in Bi_2Te_3 is europium, which has the atomic number $Z = 63$ and the electronic configuration [Xe] $4f^7$ $6s^2$. Its calculated magnetic moment is 8.8 μ_B, and it is well known to form a binary antiferromagnetic compound with Te.[22] This could increase the solubility into a Bi_2Te_3 matrix without introducing

Received: June 5, 2020
Revised: June 22, 2020
Published: June 25, 2020

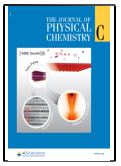

https://dx.doi.org/10.1021/acs.jpcc.0c05077
J. Phys. Chem. C 2020, 124, 16048−16057

structural disorder because Bi sites provide the same structural environment as the europium sites inside EuTe.

In this work, we present a systematic investigation of the structural and electronic properties of Eu-doped Bi_2Te_3 epitaxial layers. The films were grown by molecular beam epitaxy on (111) BaF_2 substrates with nominal Eu doping concentrations ranging from 0% (reference sample) to 9%. A first set of samples was prepared with 0, 2, 4, and 9% Eu doping. The samples consist of 100 nm-thick Bi_2Te_3:Eu films covered by a 100 nm-protective Te capping layer, which was deposited immediately after the film growth. This protective layer is intended to preserve a pristine film surface for photoemission and X-ray absorption experiments. A second set of samples with nominal Eu doping of 0, 2, and 9% consists of 25 nm-thick films grown in the same conditions but without Te capping and was meant for X-ray diffraction (XRD) investigations. The samples were characterized *in situ* by reflection high-energy electron diffraction (RHEED) and *ex situ* by XRD, scanning transmission electron microscopy (STEM), X-ray photoemission spectroscopy (XPS), X-ray absorption spectroscopy (XAS), and angle-resolved photoemission spectroscopy (ARPES). We consider several possible models for the Eu incorporation in the Bi_2Te_3 crystal matrix and contrast them with the results of the aforementioned characterization techniques. This allows us to elucidate how europium incorporates in the Bi_2Te_3 lattice as a function of doping.

The trigonal crystal lattice of Bi_2Te_3 is composed of a stacking sequence of quintuple layers (QLs) (Te^1–Bi–Te^2–Bi–Te^1) separated by van der Waals (vdW) gaps. The unit cell of the pure Bi_2Te_3 phase consists of three QLs stacked on top of each other, leading to a lattice parameter of 30.474 Å along the [0001] direction. The (0001) Bi_2Te_3 surface forms a hexagonal atomic arrangement with an in-plane lattice parameter of 4.382 Å. We chose cubic BaF_2 as the substrate to grow the Bi_2Te_3 epitaxial films because the in-plane lattice constant of its (111) surface (4.384 Å) is very close to that of Bi_2Te_3, giving an in-plane lattice mismatch of only 0.04%.[23] In principle, vdW epitaxy relaxes the lattice mismatch conditions,[24] allowing the growth of high-quality Bi_2Te_3 epitaxial layers over a wide range of substrates. However, a more accurate XRD analysis indicates that the presence of intermediate layers inside the vdW gaps, such as Bi double layers, can prevent the relaxation of the film.[25] Because this may be a scenario for magnetically doped samples, the choice of a proper substrate is of fundamental importance.

METHODS

Europium-doped bismuth telluride thin films were grown on freshly cleaved (111) barium fluoride slices using a Riber 32P molecular beam epitaxial (MBE) system. More details about the MBE growth system and sample preparation can be found elsewhere.[26] For this work, we used one effusion cell charged with nominal stoichiometric Bi_2Te_3, a second cell with the Te solid source to compensate the tellurium loss, and a third cell containing solid europium to dope the films. The beam equivalent pressure (BEP) of each cell was measured in an ion gauge just before growth. The undoped Bi_2Te_3 reference sample was grown with $BEP_{Bi_2Te_3} = 5 \times 10^{-7}$ Torr, substrate temperature $T_{SUB} = 260$ °C, and $\Phi_R = BEP_{Te}/BEP_{Bi_2Te_3} = 0.5$. These growth conditions were carefully chosen to obtain n-type bismuth telluride films close to the Bi_2Te_3 stoichiometry[27] and were found to lead to a low deposition rate and relatively low surface mobility, which reduce the chances of Eu clustering. The nominal Eu doping concentration was defined as $x_{Eu} = BEP_{Eu}/BEP_{Bi_2Te_3}$. Two sets of samples were produced. The first set with $x_{Eu} = 0\%$ (reference), 2, 4, and 9% consists of a 100 nm-thick Bi_2Te_3:Eu films covered by a 100 nm-thick protective Te capping layer, deposited just after growth, to preserve a pristine surface for photoemission and X-ray absorption experiments.[28] The second set with $x_{Eu} = 0\%$ (reference), 2, and 9% consists of 25 nm-thick films grown in the same conditions but without Te capping, which was dedicated to XRD investigation. All growths were monitored *in situ* by a RHEED system with the electron gun set to 16 kV.

X-ray reflectivity curves were simulated via recursive equations suitable for layered materials and already used to study epitaxial films of bismuth telluride.[29] Three model structures were considered for XRD simulation.

In model 1, we assume substitutional occupation of Bi sites by a concentration x of Eu in films with composition $Bi_{2(1-x)}Eu_{2x}Te_3$. Amplitudes of X-ray scattering by Bi/Eu sites were calculated as $f = (1 - x)f_{Bi} + xf_{Eu}$, where $f_A = (f_0 + f' + if'')$ is the atomic scattering factor of atom A with corrections of resonance amplitudes f' and f'' for the used X-ray energy. Because of difference in atomic radius, an increase in the atomic displacement parameters of the atoms in the Bi/Eu layers was accounted for $U = \langle \Delta u^2 \rangle + U_T$, where $\sqrt{U_T} = 19$ pm stands for thermal vibrations at room temperature[29] and $\langle \Delta u^2 \rangle = (1 - x)(r_{Bi} - \langle r \rangle)^2 + x(r_{Eu} - \langle r \rangle)^2$ is the mean-square displacement regarding the mean radius $\langle r \rangle = (1 - x)r_{Bi} + xr_{Eu}$ of the atomic radius $r_{Bi} = 154.5$ pm and $r_{Eu} = 204.2$ pm. For 2 and 9% of Eu, $x = 0.02$ and 0.09, $\sqrt{U} = 20$ and 24 pm, respectively.

In model 2, we assume interstitial occupation of Eu monolayers in the vdW gaps, films with composition $Eu_m(Bi_2Te_3)_n$. A number m of Eu monolayers distributed according to a lognormal probability in the vdW gaps of n QLs (1 monolayer per gap only). This lognormal probability is the same used to distribute Bi BLs in films with Te deficiency, as described elsewhere.[29] The interlayer distance of each occupied vdW gap changes from 2.613 Å (Te/Te) to 3.810 Å (Te/Eu/Te) because 1.905 Å is the Eu/Te atomic interlayer distance in the EuTe crystal structure at room temperature. Simulated X-ray reflectivity curves correspond to average curves over 200 model structures with $m = 1$ (0.5%), 4 (2%), 8 (4%), or 18 (9%) Eu monolayers randomly distributed in $n = 100$ QLs.

In model 3, we assume segregation of the EuTe phase in films with overall composition $(Bi_2)_m(Bi_2Te_3)_{n-m}(EuTe)_{3m}$, where a number m of QLs provides enough Te for $3m$ EuTe layers and Bi for m BLs. The Eu/Bi ratio is $3m/2n$. Simulated X-ray reflectivity curves correspond to average curves over 50 model structures with $3m = 3$ (1.5%), 6 (3%), 12 (6%), or 18 (9%) EuTe layers stacked at the bottom of the films and m Bi BLs randomly distributed in the vdW gaps of 100-m QLs stacked in the upper part of the films.

XRD measurements were done at our laboratory using a high-resolution X-ray diffractometer PANalytical X'Pert MRD equipped with a (220) Ge four-crystal monochromator, providing Cu kα_1 radiation and an open detector with total acceptance of 1°. Longitudinal Qz scans were performed at the XRD2 beamline of the Brazilian Synchrotron Light Source using a double-crystal (111) Si monochromator, with a beam

https://dx.doi.org/10.1021/acs.jpcc.0c05077
J. Phys. Chem. C 2020, 124, 16048−16057

energy of 8004 eV and a Pilatus 100k area detector. More details about the measurement configuration can be found elsewhere.[29]

Cross-sectional lamellas were prepared at the Wilhelm Conrad Röntgen Research Center for Complex Material System (RCCM) using a FEI Helios Nanolab Dual Beam system using Ga^+ ion beam milling. The lateral thickness of the lamellas is between 25 and 50 nm. STEM images were obtained using a FEI Titan 80-300 transmission electron microscope operated at 300 kV.

To perform surface analyses, the tellurium protective capping layer was mechanically removed inside ultrahigh vacuum (UHV) chambers.[28] The sample preparation consists of gluing a top-post with silver epoxy over the Te-capped films. These samples are loaded into the UHV analysis chamber and cooled down to measurement temperature. The top-post is then mechanically tilted, pulling out the Te protective capping layer and exposing pristine surfaces of Eu-doped Bi_2Te_3 samples just before measurement starts.

Core-level photoemission measurements were performed at the I09 beamline of Diamond Light Source, which delivered both soft and hard X-rays to an end-station equipped with a Scienta EW4000 electron analyzer. The two beams were directed to illuminate the same spot on the sample. The hard X-ray photon energy was set to be 5.93 keV by a Si(111) monochromator followed by a Si(004) channel-cut crystal, while the soft X-ray energy was selected by a plane-grating monochromator using a 300 line/mm grating. The sample was cooled down by a liquid He cryostat to 70 K, and the pressure stayed below 5×10^{-10} mbar throughout the measurements. The resonant photoemission experiments were carried out at the ASPHERE III endstation at beamline P04 of the PETRA III synchrotron facility at DESY (Hamburg, Germany), at a temperature of 30 K and a base pressure of 2×10^{-10} mbar.

XAS measurements were carried out at a high-field diffractometer end station of the UE46 PGM-1 beamline at BESSY II using circularly polarized photons around the Eu $M_{4,5}$ edges. Theoretical XAS spectra for the $M_{4,5}$ ($3d \rightarrow 4f$) absorption of Eu^{2+} and Eu^{3+} ions were calculated using the framework of the crystal field multiplet theory[30] and the quantum many-body script language QUANTY.[31] The hybridization effect between the localized *f*-level and conduction electrons is considered to be weak[32] and is neglected in the calculations. To account for the Eu point group in Bi_2Te_3, we describe the crystal field in O_h symmetry, thus assuming that Eu ions substitute into the lattice at cation sites, as determined by structural analysis. Contributions of the splitted ground state terms to the absorption spectra were weighted using Boltzmann factors corresponding to the experimental temperature $T = 5$ K. The calculated spectra are broadened by a Gaussian function with a standard full width of half maximum of 0.15 eV to account for the instrumental broadening and by an energy-dependent Lorentzian profile for intrinsic lifetime broadening.

ARPES measurements were performed in an ultra-high vacuum surface analysis system equipped with a Scienta R4000 hemispherical analyzer using He I_α radiation ($h\nu = 21.2$ eV). The energy resolution is better than 18 meV, and the angle resolution is 0.2°. The sample was cooled down to 20 K using liquid He. The pressure during measurement never exceeded 5×10^{-10} Torr. The second-derivative ARPES spectra were obtained by applying a Gaussian filter.

RESULTS AND DISCUSSION

In order to monitor *in situ* the growth of Eu-doped Bi_2Te_3 epilayers, RHEED patterns were acquired along the $[10\bar{1}0]$ and $[2\bar{1}\bar{1}0]$ symmetry azimuths. Figure 1 shows the RHEED

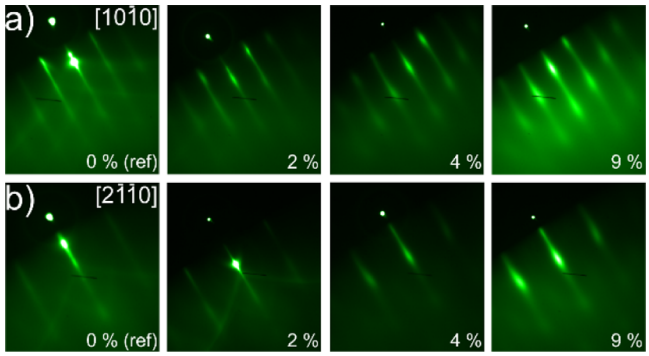

Figure 1. RHEED patterns acquired along (a) $[10\bar{1}0]$ and (b) $[2\bar{1}\bar{1}0]$ azimuthal directions for 100 nm-thick Eu-doped Bi_2Te_3 films on (111) BaF_2 substrates. The nominal Eu doping concentration ranges from 0% (reference sample) to 9%.

images along both azimuths recorded just after depositing 100 nm of Bi_2Te_3 with nominal Eu doping ranging from 0 (reference) up to 9%. For the undoped sample, a RHEED pattern composed of very thin streaks evidences a flat surface for the (0001) Bi_2Te_3 films grown on (111) BaF_2.[26] As the Eu doping level is raised, the streaks in the RHEED pattern become more elongated and wider, and the image background turns blurrier, indicating that disorder on the film surface rises with increasing Eu content.[33] The RHEED patterns shown in Figure 1 repeat for each 60° of azimuthal rotation, demonstrating that the three-fold symmetry of the Bi_2Te_3 hexagonal lattice is preserved for all samples with different Eu concentrations.[23,26] Note that the separation between streaks for RHEED patterns recorded along $[2\bar{1}\bar{1}0]$ (Figure 1b) is $\sqrt{3}$ larger than that measured along $[10\bar{1}0]$ (Figure 1a), also because of the C_{3v} symmetry. We observe no intermediate streaks for any azimuthal direction of any sample, providing evidence of the absence of surface reconstruction during these growths.

Aiming to investigate how europium atoms enter the Bi_2Te_3 crystalline structure, several model structures were used to calculate the XRD curves. Possible scenarios considered in the models are shown in Figure 2a–c. Europium atoms can enter substitutionally on Bi sites inside the QLs (Eu_{Bi} in Figure 2a); they can form Eu monolayers inside the vdW gaps (Eu_{vdW} in Figure 2b), or they can even form EuTe layers replacing QLs, as displayed in Figure 2c.

For model structures representing these three different scenarios, a computational package based on recursive equations for fast X-ray dynamical diffraction simulation in large *d*-spacing materials has been employed to generate the X-ray reflectivity curves along the [0001] growth direction.[29,34] Besides allowing simulation on wide-range Qz-scans, this computational package has been successfully applied to study $Bi_2Te_{3-\delta}$ homologous series (δ is the Te deficit in the film), where QLs and BLs can be randomly stacked along the film thickness in model structures.[28,29] We used the same approach here to randomly distribute single layers of Eu inside the vdW gaps (Eu_{vdW}). Further details of the model structures are given in the Methods section. The calculated Qz-scans for europium-

https://dx.doi.org/10.1021/acs.jpcc.0c05077
J. Phys. Chem. C 2020, 124, 16048−16057

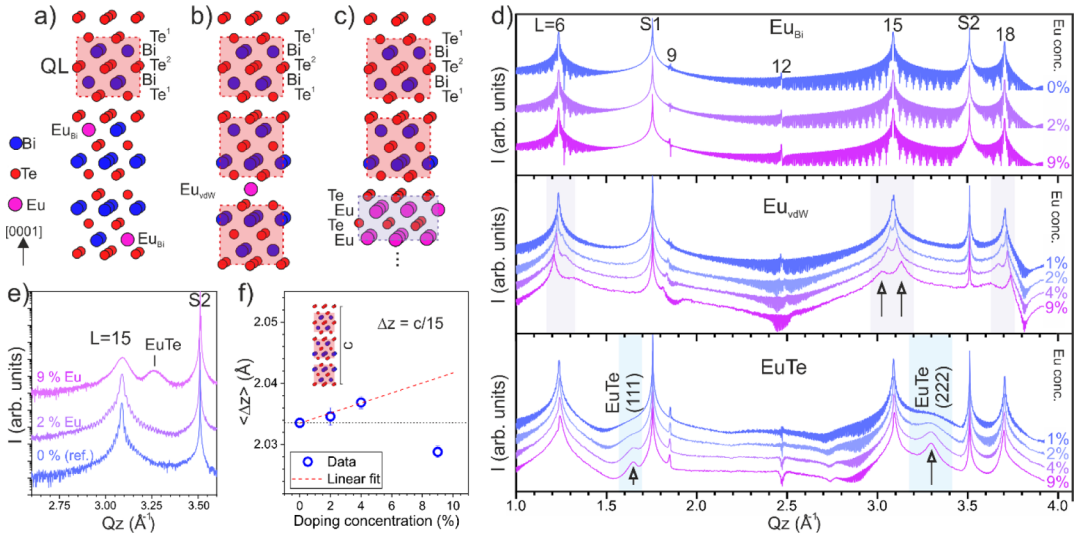

Figure 2. Possible scenarios for the incorporation of Eu in the crystal structure of Bi_2Te_3, which is composed of QLs separated by vdW gaps: (a) europium replacement of Bi ions (Eu_{Bi}), (b) randomly distributed monolayers of Eu ions accommodated inside the vdW gaps (Eu_{vdW}), and (c) clusters of EuTe layers formed in replacement of QLs. (d) Calculated XRD curves along the [0001] growth direction (Qz-scans) for the three scenarios with increasing Eu content. (e) Short-range Qz-scan measured around L = 15 Bi_2Te_3 and (222) BaF_2 Bragg peaks. (f) Mean interplanar atomic distance $\langle \Delta z \rangle$ extracted from the measured L = 15 Bi_2Te_3 peak as a function of Eu-doping concentration. The red dashed line is a linear fit for the Eu content up to 4%. The black dotted line indicates the $\langle \Delta z \rangle$ value of undoped Bi_2Te_3.

entering Bi sites (Eu_{Bi}), being incorporated inside the vdW gap (Eu_{vdW}) or forming secondary EuTe phase, are shown in the upper, middle, and lower panel of Figure 2d, respectively. In all these curves, S1 and S2 labels correspond to the (111) and (222) Bragg peaks of the BaF_2 substrate, respectively.

For the pure Bi_2Te_3 pattern, because the nonprimitive unit cell is composed of three QLs, only the (000L) Bragg peaks with L being a multiple of 3 are visible. The weak intensity of the peaks for L = 9 and 12 is because of their low structure factors.[29,35] By randomly replacing Bi atoms with Eu, the calculated curves preserve the Bi_2Te_3 peak position and shape. No splitting is observed in the Bi_2Te_3 diffraction peaks, even for the 9% Eu-doped film. By increasing the amount of Eu in the structure, the intensity of the diffraction peaks and the amplitude of the interference fringes decrease. A slight change can be observed for the peaks L = 9 and 12, in which the phase inversion is enhanced for increasing Eu concentration. However, because the intensity difference to (111) BaF_2 diffraction peak is around 6 orders of magnitude, the signal-to-noise ratio around these Bi_2Te_3 diffraction peaks is too low even when using a synchrotron light source.

For Eu atoms residing in the vdW gaps, with nominal Eu concentration ranging from 1% up to 9%, the Bi_2Te_3 Bragg peaks are directly modified. The most clear signature is a splitting of the L = 15 Bi_2Te_3 Bragg peak, which is the bismuth telluride peak with the highest structure factor.[35] The splitting is indicated in the figure by two short arrows. The peak separation increases linearly with increasing Eu concentration, appearing clearly even for the 1% Eu-doped curve. Less-pronounced splittings can also be observed for the peaks L = 6 and L = 18 in the direction of higher and lower Qz values, respectively.

The calculated diffraction curves for Bi_2Te_3 films mixed with the EuTe phase are shown in the lower panel of Figure 2d for a nominal Eu doping concentration ranging from 1 to 9%. For this scenario, EuTe layers oriented along the [111] direction are inserted in between Bi_2Te_3 QLs with thickness matching the nominal doping. The calculated curves clearly show the appearance of extra diffraction peaks around Qz = 1.65 and 3.3 $Å^{-1}$, which are related to the (111) and (222) Bragg peaks of the EuTe epitaxial phase, respectively. These secondary-phase diffraction peaks appear as faint shoulders for Eu concentrations equal to 1% and become more intense and visible as the Eu content is raised up to 9%. The calculated curves exhibit no significant change for any of the Bi_2Te_3 diffraction peaks. The presence of interference fringes is suppressed with increasing Eu concentration, which is a consequence of broken periodicity in the crystal lattice.[29]

To evaluate experimentally the effect of Eu doping in the Bi_2Te_3 epitaxial films, Qz scans were acquired along the [0001] direction at the XRD2 beamline of the Brazilian Synchrotron Light Source. Because the most significant effects in the XRD curves should occur in the vicinity of the L = 15 Bi_2Te_3 Bragg peak, Qz scans were acquired around this region. Figure 2e shows short-range Qz scans around the L = 15 Bi_2Te_3 and (222) BaF_2 diffraction peaks for samples with different Eu concentrations. The curve of the 2% Eu-doped sample exhibits no splitting and no extra diffraction peak in comparison to the undoped sample, indicating that Eu atoms enter substitutionally on Bi sites inside the QLs for this doping level. For the 9% Eu-doped sample, an extra diffraction peak is visible at Qz = 3.261 $Å^{-1}$. This peak corresponds to the calculated peak of the (222) EuTe phase, evidencing the formation of an epitaxial secondary phase grown with the (111) EuTe plane parallel to the (111) BaF_2 basal plane. The extracted d-spacing for the (222) EuTe diffraction peak is d = 1.927 Å, which is higher than the bulk value (d = 1.905 Å), indicating that the EuTe layers embedded in the Bi_2Te_3 matrix are strained. In addition, the undoped and the 2% Eu-doped curves exhibit well-defined interference fringes, indicating homogeneous and ordered layers along the whole substrate area. In contrast, the 9% Eu-doped sample exhibits an increase of the full width at half-maximum for the L = 15 Bi_2Te_3 diffraction peak and the interference fringes are no longer observable. This suggests

https://dx.doi.org/10.1021/acs.jpcc.0c05077
J. Phys. Chem. C 2020, 124, 16048−16057

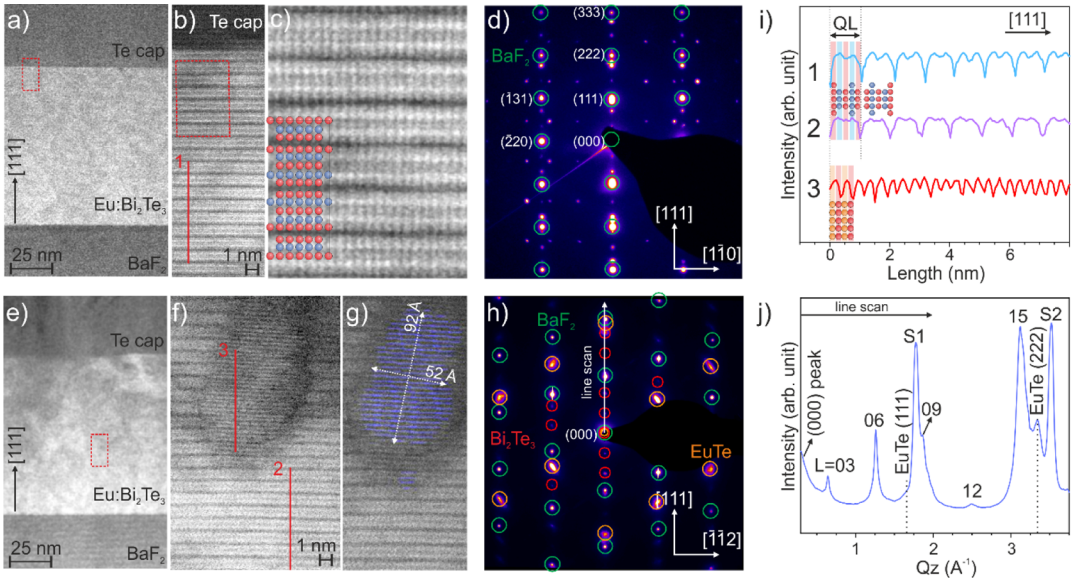

Figure 3. Scanning transmission electron microscopy cross-section images of 100 nm-thick Eu-doped Bi_2Te_3 epitaxial films (covered with Te capping layer) with 2 and 9% of nominal Eu concentrations. The images for the 2 and 9% Eu-doped samples were taken along [1 −1 0] and [−1 −1 2] BaF_2 azimuthal directions, respectively. (a) Cross-section image of the 2% Eu-doped sample showing clearly the BaF_2 substrate, the 100 nm-thick Bi_2Te_3:Eu film, and the Te protective layer. (b) Zoom into the red rectangle of (a) shows the 18 topmost QLs separated by vdW gaps (darker lines parallel to the sample surface) together with the Te cap layer. (c) Augmented image for the 6 upper QLs [zoom into the red rectangle of (b)] exhibiting well-defined QLs intercalated with vdW gaps, demonstrating that the Bi_2Te_3 lattice matrix is preserved up to the Te-cap interface. (d) Diffraction pattern obtained from the 2% Eu-doped sample. The green circles correspond to the calculated position of BaF_2 peaks, while the others are related to Bi_2Te_3. (e) Cross-section image of the 9% Eu-doped sample showing the substrate, smudgy film, and Te capping. (f) Zoom into the red rectangle of (e) showing a crystalline EuTe cluster embedded in the Bi_2Te_3 lattice. (g) Composite image obtained from a Fourier transform, highlighting the EuTe cluster in blue. (h) Diffraction pattern obtained from the 9% Eu-doped sample. Green, red, and orange circles correspond to the calculated positions of BaF_2, Bi_2Te_3, and EuTe, respectively. (i) Intensity profile along the line 1 in (b) and lines 2 and 3 in (f). (j) Diffracted intensity as a function of Qz extracted along the white line in (h). The line scan shows, besides the S1 and S2 substrate peaks, the L = 03, 06, 09, 12, and 15 peaks related to the Bi_2Te_3 phase and clear extra diffraction peaks corresponding to EuTe.

that the Bi_2Te_3 matrix has domains with significant differences in thickness.

The mean interplanar atomic distance ($\langle \Delta z \rangle$) was measured for all Te-capped samples. By measuring the position of the L = 15 Bi_2Te_3 Bragg peak, it is possible to calculate the unit cell height c. The mean interplanar atomic distance is equal to c/15. The result is shown in Figure 2e as a function of nominal Eu concentration. The open circles indicate the experimental values, and the red dotted line represents the linear fit to the data excluding the 9% Eu-doped sample. The Te deficit in the $Bi_2Te_{3-\delta}$ phase because of formation of the EuTe phase can be one of the reasons for the observed reduction in $\langle \Delta z \rangle$ for the 9% Eu-doped sample. By adding europium to bismuth telluride, the mean interplanar atomic distance presents a linear increase up to 4% of nominal Eu doping, which agrees with europium atoms replacing bismuth positions because Eu^{2+} (Eu^{3+}) has an ionic radius equal to 1.17 Å (0.95 Å), while the ionic radius of Bi^{3+} is 1.03 Å.[36] This linear increase in $\langle \Delta z \rangle$ suggests a homogeneous incorporation of Eu atoms in the form of Eu^{2+}, rather than Eu^{3+}, into the Bi sites of the Bi_2Te_3 lattice. The linear increase of the mean interplanar atomic distance together with the simulated and measured XRD curves reinforces the hypothesis that Eu replaces Bi up to 4% of nominal doping. A linear change in the out-of-plane lattice constant was previously also observed for homogeneous Cr incorporation into bismuth-antimony telluride samples up to 8% of nominal Cr concentration. Above this value, a secondary Cr_2Te_3 phase was observed.[37]

STEM was employed to gain further insights into the structure of Eu-doped Bi_2Te_3 epilayers. Figure 3a presents a cross-section STEM image of the 2% Eu-doped bismuth telluride epitaxial film, which shows the BaF_2 substrate, the 100 nm-thick film, and the Te capping layer. By zooming into the red rectangle of Figure 3a, one can distinguish the 18 topmost QLs together with the Te protective layer, as shown in Figure 3b. In this image, the QLs are clearly visible separated by vdW gaps that appear as darker lines parallel to the sample surface. The presence of well-defined QLs intercalated with vdW gaps indicates that the Bi_2Te_3 lattice matrix is preserved up to the Te-cap interface, as demonstrated by the augmented image for the 6 upper QLs in Figure 3c obtained from the zoom into the red rectangle of Figure 3b. The diffraction pattern obtained for the 2% Eu-doped sample is presented in Figure 3d. The green circles indicate the calculated position of the BaF_2 peaks. The remaining diffraction points are purely because of the Bi_2Te_3 structure. The STEM images show no evidence of secondary phases in the films with Eu doping up to 4%, corroborating the XRD analysis.

The cross-section STEM image acquired for the 9% Eu-doped Bi_2Te_3 sample is shown in Figure 3e with an overview of the substrate, the film, and the Te capping layer. The smudgy image of the epitaxial film indicates an inhomogeneous Eu-doped bismuth telluride layer. By zooming into the red rectangle of Figure 3e, we obtain the image in Figure 3f. In this image, one can see a cluster with a different atomic arrangement, embedded in the Bi_2Te_3 matrix, which we identify as an EuTe cluster. In order to better visualize the cluster, a two-dimensional Fourier transform is applied, the frequencies related to the Bi_2Te_3 QLs are removed, and the original image is recovered by applying an inverse transform.

https://dx.doi.org/10.1021/acs.jpcc.0c05077
J. Phys. Chem. C 2020, 124, 16048−16057

Figure 3g shows the composite image with the region extracted from the Fourier transform highlighted in blue. In this composite image, it is clear that this cluster presents a different crystalline arrangement. The extracted mean interatomic plane distance for this region is approximately 1.8 Å, lower than the pure Bi_2Te_3 mean interatomic planar distance (2.03 Å).[26] Figure 3h shows the diffraction pattern obtained from the 9% Eu-doped sample. The green, red, and orange circles indicate the calculated position of the BaF_2, Bi_2Te_3, and EuTe peaks, respectively. The pattern of this sample shows distinctly extra spots corresponding to the EuTe phase.

Figure 3j depicts the diffracted intensity versus Qz extracted along the white line in Figure 3h. In this graph, besides the S1 and S2 Bragg peaks, corresponding to the (111) and (222) BaF_2 substrate peaks, Bi_2Te_3 and EuTe peaks are also visible. The Bi_2Te_3 (000L) Bragg peaks with L = 03, 06, 09, 12, and 15 are identified in the graph, and dotted lines indicate the (111) and (222) EuTe peaks. The (111) EuTe reflection appears as a faint shoulder close to S1 because of a smaller structure factor, while the (222) EuTe peak is clearly visible between the peaks L = 15 and S2.

The intensity profile along line 1 in Figure 3b and the lines 2 and 3 in Figure 3f are shown in Figure 3i. Because of parallax effects, the mean interplanar atomic distances cannot be precisely determined. However, for the 9% Eu-doped sample, it is clear that the nanoclusters present a smaller mean interplane atomic distance when directly compared to the Bi_2Te_3 QLs. A mean interplanar atomic spacing of 1.8 Å inside the EuTe agglomerate is found.

EuTe crystallizes in the cubic rock-salt structure with a lattice parameter of 6.598 Å. The in-plane lattice constant of its (111) surface (4.665 Å) is larger by 6.42% than the in-plane lattice parameter of hexagonal Bi_2Te_3 (4.382 Å), which is a considerable lattice mismatch. In spite of this large mismatch, our findings demonstrate that well-ordered crystalline EuTe clusters can coexist within the Bi_2Te_3 matrix. This astonishing result can be explained by the capacity of the Bi_2Te_3 lattice to accommodate large strain values in the vdW gaps between the QLs. The vdW epitaxy between Bi_2Te_3 and highly lattice mismatched materials (up to 19%) has been already demonstrated,[38] resulting in preserved Bi_2Te_3 QLs with atomically sharp interfaces and no misfit dislocations. Our results open up the possibility to investigate both homogeneous magnetically doped bismuth telluride thin films and epitaxial bismuth telluride films with embedded EuTe antiferromagnetic nanoclusters.

All results from XRD and STEM analyses confirm unambiguously that in the 9% Eu-doped sample, a secondary EuTe phase is formed. These clusters of EuTe grow epitaxially in the Bi_2Te_3 matrix with the (111) EuTe plane oriented parallel to the (0001) Bi_2Te_3 basal plane. Further investigations using XPS, XAS, and ARPES were done to better understand the mechanisms of the europium incorporation in bismuth telluride.

To perform XPS, XAS, and ARPES, the Te protective capping layer was mechanically removed inside the surface analysis vacuum chamber, which has already been proved to be a very efficient and simple technique to preserve pristine surfaces.[28] Figure 4a presents the XPS spectrum acquired at the Eu 4d core level for the 4% Eu-doped Bi_2Te_3 thin film using a photon energy of $h\nu$ = 5.9 keV to increase bulk sensitivity. A well-resolved multiplet structure of the Eu 4d core level is observed, which is characteristic of the exchange

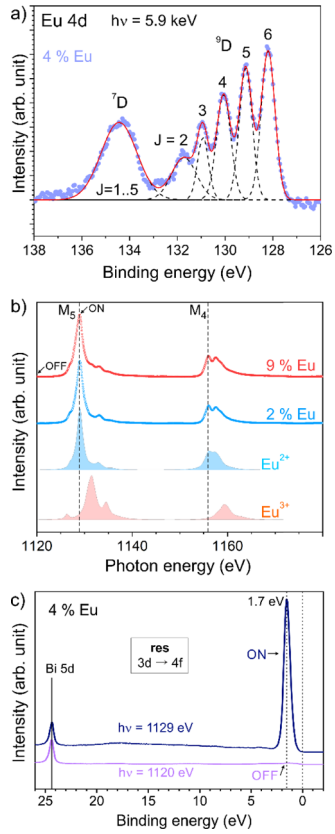

Figure 4. (a) X-ray photoelectron spectrum of the Eu 4d core level measured for a 4% Eu-doped Bi_2Te_3 film with photon energy $h\nu$ = 5.9 keV at 70 K. The dashed lines are pseudo-Voigt fits to the observed peaks, and the solid red line is the sum of all curves that best fitted to the experimental data. A Shirley background correction was applied. (b) X-ray absorption spectra measured at the Eu $M_{4,5}$ edges of the 2 and 9% Eu-doped (0001) Bi_2Te_3 films at 5 K together with calculated Eu^{2+} and Eu^{3+} XAS spectral curves. (c) Spectra of the 4% Eu-doped sample obtained by resonant excitation at photon energies near the Eu 3d to 4f absorption edge. Small arrows at figure (b) indicate the excitation energies near the Eu M_5 absorption edge.

splitting of the Eu^{2+} ($^8S_{7/2}$) valence state.[39] The various final states ^9D_J with J = 2, 3, 4, 5, and 6 can be clearly distinguished, evidencing that Eu is in a divalent state in Bi_2Te_3 epitaxial films.[40,41] The multiplet structure ^7D_J with J = 1−5 appears as an unresolved manifold at higher binding energies. An increase of the full width at half-maximum with a corresponding decrease of peak intensity as a function of increasing binding energy has been already observed for other RE 4d spectra.[42] In the case of Eu^{3+}, the 4d levels would appear at higher binding energies.[40] Similar results were observed for the spectrum acquired for the 9% Eu-doped Bi_2Te_3 sample and with photon energy of $h\nu$ = 1.2 keV to increase surface sensitivity (not shown here). Our XPS results demonstrate that the Eu atoms are entering the bismuth telluride matrix with the same Eu^{2+} valence as in the EuTe clusters.

Figure 4b shows XAS spectra measured at the Eu $M_{4,5}$ edges for the 2 and 9% Eu-doped Bi_2Te_3 films (top curves) and the calculated spectra of Eu^{2+} and Eu^{3+} (bottom curves). The measurements were conducted at T = 5 K. The XAS line shape is the same for all three samples (4% Eu-doped not shown here) and shows an overwhelming prevalence of Eu^{2+}.[30,43] The results obtained by the XPS and XAS analyses thus demonstrate unequivocally that Eu atoms enter into the

https://dx.doi.org/10.1021/acs.jpcc.0c05077
J. Phys. Chem. C 2020, 124, 16048−16057

Bi_2Te_3 lattice as Eu^{2+}. In addition, previous transport results on Eu-doped Bi_2Te_3 bulk crystals have shown an increase of p-type doping with rising europium content,[44] which is also indicative of Eu atoms replacing Bi with less valence electrons.

Presence of the divalent Eu in our samples is in line with the general tendency of binary compounds of Eu and the elements of group 6 to stabilize the lower oxidation state of Eu with heavier and less electronegative chalcogens. The trivalent state is the most stable in oxides, for instance, in $Eu_2^{III}O_3$ with the highest melting point of 2573 K, whereas the $Eu^{II}O$ phase decomposes at 1793 K.[45] Decreasing electronegativity and increasing polarizability in the S−Se−Te series progressively favors the divalent state. EuS is already more stable, with a higher melting point, than the mixed-valence compound Eu_3S_4, and, moreover, only divalent EuSe and EuTe are stable for heavy chalcogens.[45]

To probe the location of the Eu 4f levels in the valence band, Eu 3d to 4f resonant photoemission experiments were performed, as shown in Figure 4c. The photon energies for the on—(1129 eV) and off—(1120 eV) resonance were chosen based on the XAS spectrum, as indicated by short arrows in Figure 4b. A clear sharp single peak of Eu 4f is observed at *ca.* 1.7 eV below the Fermi energy.

To consider the effect of Eu dopants on the surface electronic structure, we measured ARPES in the vicinity of the $\bar{\Gamma}$ point of all Eu-doped Bi_2Te_3 thin films. Figure 5a shows the

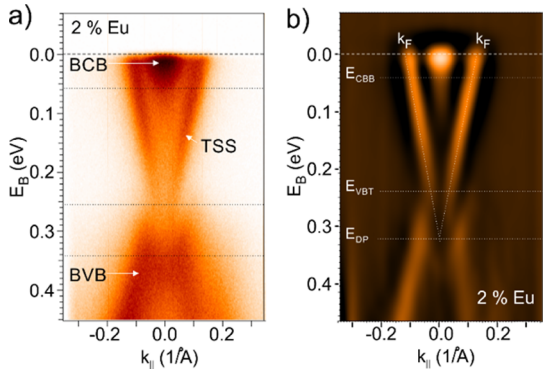

Figure 5. (a) ARPES spectrum near the $\bar{\Gamma}$ point of the Bi_2Te_3 epitaxial film doped with 2% of Eu acquired at 20 K with a photon energy of $h\nu$ = 21.2 eV. (b) Second-derivative intensity plot with Gaussian smoothing obtained from the respective ARPES spectra. The dashed lines serve as guide to the eye of the TSS dispersion.

ARPES spectrum measured on the (0001) Bi_2Te_3 surface of the 2% Eu-doped sample. ARPES measurements for higher doping levels yielded similar results, albeit with additional broadening because of the increased disorder. The measurement was performed using He Iα radiation ($h\nu$ = 21.2 eV) right after the mechanical removal of the protective Te capping layer at 20 K. The M-shaped bulk valence band and the bulk conduction band are clearly visible, in close analogy to pristine Bi_2Te_3.[28] Moreover, the dispersion of the TSS is clearly observed, indicating that the topological surface remains robust in the presence of local Eu magnetic moments for all investigated doping levels. Based on our data, we can also exclude the occurrence of sizable gaps in the TSS on the order of 50−100 meV, as they were observed for Mn-, Fe-, and V-doped bismuth chalcogenides.[5,17,46]

The boundaries of the energy bands can be seen in a clearer way by analyzing the second-derivative images of the raw ARPES spectrum. The second-derivative intensity plot is shown in Figure 5b and was obtained using Gaussian smoothing with a width equal to 0.06 and 0.07 for d/dx and d/dy, respectively. The d/dy image was scaled down to 15%. From our ARPES data, we estimated the group velocity (v_g) of the TSS to be 2.55 eV/Å (3.9×10^5 m/s). This value is in very good agreement with previous values reported for pristine Bi_2Te_3 bulk samples.[19]

Previously, the gap opening in Mn-doped Bi_2Se_3 has been attributed to resonant Mn 3d states near the Dirac point.[17] In the present case, our resonant photoemission data in Figure 4c show negligible Eu 4f spectral weight near the Fermi level. In this regard, our data are consistent with the scenario, showing a gapless TSS in the absence of impurity states close in energy.

CONCLUSIONS

We have investigated the incorporation of Eu in Bi_2Te_3 TI films. To this purpose, two sets of Eu-doped Bi_2Te_3 layers were grown on (111) BaF_2 substrates by molecular beam epitaxy with nominal Eu content varying from 0% (reference) to 9%. *In situ* RHEED analysis demonstrated that all films grow in a layer-by-layer mode since the early stages. Additionally, we observe no surface reconstruction or increase of the surface disorder with increasing Eu doping. Three possible scenarios were considered for the incorporation of Eu in the crystal matrix of Bi_2Te_3: (i) Eu atoms entering substitutionally in Bi sites; (ii) single Eu layers being incorporated in the vdW gaps, and (iii) EuTe phase formation in clusters. XRD calculations and measurements together with STEM images revealed that Eu atoms enter substitutionally in Bi positions up to 4% of Eu doping, and that for the 9% Eu-doped sample EuTe crystalline clusters (5−10 nm in dimension) are formed, embedded in the Bi_2Te_3 lattice with the (111) EuTe plane parallel to the (0001) Bi_2Te_3 basal plane. The XPS and XAS results proved that Eu atoms are entering into the Bi_2Te_3 lattice in the divalent Eu^{2+} state. Our ARPES experiments show that the TSS remains robust and gapless in the presence of the Eu-induced local magnetic moments.

AUTHOR INFORMATION

Corresponding Author

Celso I. Fornari − *Experimentelle Physik VII and Würzburg-Dresden Cluster of Excellence ct.qmat, Fakultät für Physik und Astronomie, Universität Würzburg, Würzburg D-97074, Germany; Laboratório Associado de Sensores e Materiais, Instituto Nacional de Pesquisas Espaciais, São José dos Campos 12245-970, São Paulo, Brazil;* orcid.org/0000-0003-1765-2999; Email: celso.fornari@physik.uni-wuerzburg.de

Authors

Hendrik Bentmann − *Experimentelle Physik VII and Würzburg-Dresden Cluster of Excellence ct.qmat, Fakultät für Physik und Astronomie, Universität Würzburg, Würzburg D-97074, Germany*

Sérgio L. Morelhão − *Instituto de Física, Universidade de São Paulo, São Paulo 05508-090, Brazil;* orcid.org/0000-0003-1643-0948

Thiago R. F. Peixoto − *Experimentelle Physik VII and Würzburg-Dresden Cluster of Excellence ct.qmat, Fakultät für Physik und Astronomie, Universität Würzburg, Würzburg D-97074, Germany*

https://dx.doi.org/10.1021/acs.jpcc.0c05077
J. Phys. Chem. C 2020, 124, 16048−16057

Paulo H. O. Rappl − *Laboratório Associado de Sensores e Materiais, Instituto Nacional de Pesquisas Espaciais, São José dos Campos 12245-970, São Paulo, Brazil*
Abdul-Vakhab Tcakaev − *Experimentelle Physik IV, Universität Würzburg, Würzburg D-97074, Germany*
Volodymyr Zabolotnyy − *Experimentelle Physik IV, Universität Würzburg, Würzburg D-97074, Germany*
Martin Kamp − *Physikalisches Institut and Röntgen-Center for Complex Material Systems (RCCM), Fakultät für Physik und Astronomie, Universität Würzburg, Würzburg D-97074, Germany*
Tien-Lin Lee − *Diamond Light Source, Didcot OX11 0DE, U.K.*
Chul-Hee Min − *Experimentelle Physik VII and Würzburg-Dresden Cluster of Excellence ct.qmat, Fakultät für Physik und Astronomie, Universität Würzburg, Würzburg D-97074, Germany*
Philipp Kagerer − *Experimentelle Physik VII and Würzburg-Dresden Cluster of Excellence ct.qmat, Fakultät für Physik und Astronomie, Universität Würzburg, Würzburg D-97074, Germany*
Raphael C. Vidal − *Experimentelle Physik VII and Würzburg-Dresden Cluster of Excellence ct.qmat, Fakultät für Physik und Astronomie, Universität Würzburg, Würzburg D-97074, Germany*
Anna Isaeva − *Faculty of Physics and Würzburg-Dresden Cluster of Excellence ct.qmat, Technische Universität Dresden, Dresden D-01062, Germany; Leibniz IFW Dresden and Würzburg-Dresden Cluster of Excellence ct.qmat, Dresden D-01069, Germany;* orcid.org/0000-0001-6590-1393
Michael Ruck − *Faculty of Chemistry and Food Chemistry, Technische Universität Dresden, Dresden D-01062, Germany; Max Planck Institute for Chemical Physics of Solids and Würzburg-Dresden Cluster of Excellence ct.qmat, Dresden D-01187, Germany;* orcid.org/0000-0002-2391-6025
Vladimir Hinkov − *Experimentelle Physik IV, Universität Würzburg, Würzburg D-97074, Germany*
Friedrich Reinert − *Experimentelle Physik VII and Würzburg-Dresden Cluster of Excellence ct.qmat, Fakultät für Physik und Astronomie, Universität Würzburg, Würzburg D-97074, Germany*
Eduardo Abramof − *Laboratório Associado de Sensores e Materiais, Instituto Nacional de Pesquisas Espaciais, São José dos Campos 12245-970, São Paulo, Brazil*

Complete contact information is available at: https://pubs.acs.org/10.1021/acs.jpcc.0c05077

Notes

The authors declare no competing financial interest.

■ ACKNOWLEDGMENTS

This work was supported by the German Research Foundation (DFG) in the framework of the Würzburg-Dresden Cluster of Excellence on Complexity and Topology in Quantum Matter-ct.qmat (EXC 2147, Project-ID 390858490), Project-ID 258499086-SFB 1170 (projects A01, C04, and C06), and BMBF Project-ID 05K19WW2. This work was also supported by CNPq (grant nos. 142191/2014-0, 305764/2018-7, 309867/2017-7, 307933/2013-0, and 306982/2012-9) and FAPESP (grant nos. 2014/04150-0, 2016/22366-5, and 2019/01946-1). The authors acknowledge LNLS (proposal no. XRD2-20150037), Diamond Light Source beamline I09. Parts of this research were carried out at PETRA III (DESY, Hamburg, Germany) under Proposal No. I-20181060. We would like to thank Florian Diekmann, Sebastian Rohlf, Matthias Kalläne, and the staff of beamline P04 for experimental support. We would like to thank Eugen Weschke and Enrico Schierle for assistance during the experiment. We thank HZB for the allocation of synchrotron radiation beamtime and thankfully acknowledge the financial support from HZB. C.I.F. acknowledges the Hallwachs-Röntgen Postdoc Program of ct.qmat for financial support.

■ REFERENCES

(1) Nomura, K.; Nagaosa, N. Surface-Quantized Anomalous Hall Current and the Magnetoelectric Effect in Magnetically Disordered Topological Insulators. *Phys. Rev. Lett.* **2011**, *106*, 166802.
(2) Yu, R.; Zhang, W.; Zhang, H.-J.; Zhang, S.-C.; Dai, X.; Fang, Z. Quantized Anomalous Hall Effect in Magnetic Topological Insulators. *Science* **2010**, *329*, 61−64.
(3) Qi, X.-L.; Li, R.; Zang, J.; Zhang, S.-C. Inducing a Magnetic Monopole with Topological Surface States. *Science* **2009**, *323*, 1184−1187.
(4) Tse, W.-K.; MacDonald, A. H. Giant Magneto-Optical Kerr Effect and Universal Faraday Effect in Thin-Film Topological Insulators. *Phys. Rev. Lett.* **2010**, *105*, 057401.
(5) Chen, Y. L.; Chu, J. H.; Analytis, J. G.; Liu, Z. K.; Igarashi, K.; Kuo, H.-H.; Qi, X. L.; Mo, S. K.; Moore, R. G.; Lu, D. H.; Hashimoto, M.; Sasagawa, T.; Zhang, S. C.; Fisher, I. R.; Hussain, Z.; Shen, Z. X. Massive Dirac Fermion on the Surface of a Magnetically Doped Topological Insulator. *Science* **2010**, *329*, 659−662.
(6) Wray, L. A.; Xu, S.-Y.; Xia, Y.; Hsieh, D.; Fedorov, A. V.; Hor, Y. S.; Cava, R. J.; Bansil, A.; Lin, H.; Hasan, M. Z. A Topological Insulator Surface under Strong Coulomb, Magnetic and Disorder Perturbations. *Nat. Phys.* **2011**, *7*, 32−37.
(7) Hor, Y. S.; Roushan, P.; Beidenkopf, H.; Seo, J.; Qu, D.; Checkelsky, J. G.; Wray, L. A.; Hsieh, D.; Xia, Y.; Xu, S.-Y.; Qian, D.; Hasan, M. Z.; Ong, N. P.; Yazdani, A.; Cava, R. J. Development of ferromagnetism in the doped topological insulator Bi 2- x Mn x Te 3. *Phys. Rev. B: Condens. Matter Mater. Phys.* **2010**, *81*, 195203.
(8) Zhang, J.; Chang, C.-Z.; Tang, P.; Zhang, Z.; Feng, X.; Li, K.; Wang, L.-l.; Chen, X.; Liu, C.; Duan, W.; He, K.; Xue, Q.-K.; Ma, X.; Wang, Y. Topology-Driven Magnetic Quantum Phase Transition in Topological Insulators. *Science* **2013**, *339*, 1582−1586.
(9) Chang, C.-Z.; Zhang, J.; Feng, X.; Shen, J.; Zhang, Z.; Guo, M.; Li, K.; Ou, Y.; Wei, P.; Wang, L.-L.; Ji, Z.-Q.; Feng, Y.; Ji, S.; Chen, X.; Jia, J.; Dai, X.; Fang, Z.; Zhang, S.-C.; He, K.; Wang, Y.; Lu, L.; Ma, X.-C.; Xue, Q.-K. Experimental Observation of the Quantum Anomalous Hall Effect in a Magnetic Topological Insulator. *Science* **2013**, *340*, 167−170.
(10) Otrokov, M. M.; Klimovskikh, I. I.; Bentmann, H.; Estyunin, D.; Zeugner, A.; Aliev, Z. S.; Gaß, S.; Wolter, A. U. B.; Koroleva, A. V.; Shikin, A. M.; Blanco-Rey, M.; Hoffmann, M.; Rusinov, I. P.; Vyazovskaya, A. Y.; Eremeev, S. V.; Koroteev, Y. M.; Kuznetsov, V. M.; Freyse, F.; Sánchez-Barriga, J.; Amiraslanov, I. R.; Babanly, M. B.; Mamedov, N. T.; Abdullayev, N. A.; Zverev, V. N.; Alfonsov, A.; Kataev, V.; Büchner, B.; Schwier, E. F.; Kumar, S.; Kimura, A.; Petaccia, L.; Di Santo, G.; Vidal, R. C.; Schatz, S.; Kißner, K.; Ünzelmann, M.; Min, C. H.; Moser, S.; Peixoto, T. R. F.; Reinert, F.; Ernst, A.; Echenique, P. M.; Isaeva, A.; Chulkov, E. V. Prediction and Observation of an Antiferromagnetic Topological Insulator. *Nature* **2019**, *576*, 416−422.
(11) Vidal, R. C.; Zeugner, A.; Facio, J. I.; Ray, R.; Haghighi, M. H.; Wolter, A. U. B.; Bohorquez, L. T. C.; Caglieris, F.; Moser, S.; Figgemeier, T.; Peixoto, T. R. F.; Vasili, H. B.; Valvidares, M.; Jung, S.; Cacho, C.; Alfonsov, A.; Mehlawat, K.; Kataev, V.; Hess, C.; Richter, M.; Büchner, B.; van den Brink, J.; Ruck, M.; Reinert, F.; Bentmann, H.; Isaeva, A. Topological Electronic Structure and Intrinsic Magnetization in MnBi4Te7: A Bi2Te3 Derivative with a Periodic Mn Sublattice. *Phys. Rev. X* **2019**, *9*, 41065.

(12) Vidal, R. C.; Bentmann, H.; Peixoto, T. R. F.; Zeugner, A.; Moser, S.; Min, C.-H.; Schatz, S.; Kißner, K.; Ünzelmann, M.; Fornari, C. I.; Vasili, H. B.; Valvidares, M.; Sakamoto, K.; Mondal, D.; Fujii, J.; Vobornik, I.; Jung, S.; Cacho, C.; Kim, T. K.; Koch, R. J.; Jozwiak, C.; Bostwick, A.; Denlinger, J. D.; Rotenberg, E.; Buck, J.; Hoesch, M.; Diekmann, F.; Rohlf, S.; Kalläne, M.; Rossnagel, K.; Otrokov, M. M.; Chulkov, E. V.; Ruck, M.; Isaeva, A.; Reinert, F. Surface States and Rashba-Type Spin Polarization in Antiferromagnetic MnBi2Te4 (0001). *Phys. Rev. B* **2019**, *100*, 121104.

(13) Chen, Y. J.; Xu, L. X.; Li, J. H.; Li, Y. W.; Wang, H. Y.; Zhang, C. F.; Li, H.; Wu, Y.; Liang, A. J.; Chen, C.; Jung, S. W.; Cacho, C.; Mao, Y. H.; Liu, S.; Wang, M. X.; Guo, Y. F.; Xu, Y.; Liu, Z. K.; Yang, L. X.; Chen, Y. L. Topological electronic structure and its temperature evolution in antiferromagnetic topological insulator MnBi 2 Te 4. *Phys. Rev. X* **2019**, *9*, 041040.

(14) Deng, Y.; Yu, Y.; Shi, M. Z.; Guo, Z.; Xu, Z.; Wang, J.; Chen, X. H.; Zhang, Y. Quantum Anomalous Hall Effect in Intrinsic Magnetic Topological Insulator MnBi 2 Te 4. *Science* **2020**, *367*, 895−900.

(15) Liu, C.; Wang, Y.; Li, H.; Wu, Y.; Li, Y.; Li, J.; He, K.; Xu, Y.; Zhang, J.; Wang, Y. Robust Axion Insulator and Chern Insulator Phases in a Two-Dimensional Antiferromagnetic Topological Insulator. *Nat. Mater.* **2020**, *19*, 522−527.

(16) Mong, R. S. K.; Moore, J. E. Magnetic and Topological Order United in a Crystal. *Nature* **2019**, *576*, 390−392.

(17) Sánchez-Barriga, J.; Varykhalov, A.; Springholz, G.; Steiner, H.; Kirchschlager, R.; Bauer, G.; Caha, O.; Schierle, E.; Weschke, E.; Ünal, A. A.; Valencia, S.; Dunst, M.; Braun, J.; Ebert, H.; Minár, J.; Golias, E.; Yashina, L. V.; Ney, A.; Holý, V.; Rader, O. Nonmagnetic Band Gap at the Dirac Point of the Magnetic Topological Insulator (Bi1−xMnx)2Se3. *Nat. Commun.* **2016**, *7*, 10559.

(18) Xu, S.-Y.; Neupane, M.; Liu, C.; Zhang, D.; Richardella, A.; Wray, L. A.; Alidoust, N.; Leandersson, M.; Balasubramanian, T.; Sánchez-Barriga, J.; Rader, O.; Landolt, G.; Slomski, B.; Dil, J. H.; Osterwalder, J.; Chang, T.-R.; Jeng, H.-T.; Lin, H.; Bansil, A.; Samarth, N.; Hasan, M. Z. Hedgehog Spin Texture and Berry's Phase Tuning in a Magnetic Topological Insulator. *Nat. Phys.* **2012**, *8*, 616−622.

(19) Chen, Y. L.; Analytis, J. G.; Chu, J.-H.; Liu, Z. K.; Mo, S.-K.; Qi, X. L.; Zhang, H. J.; Lu, D. H.; Dai, X.; Fang, Z.; Zhang, S. C.; Fisher, I. R.; Hussain, Z.; Shen, Z.-X. Experimental Realization of a Three-Dimensional Topological Insulator Bi2Te3. *Science* **2009**, *325*, 178−181.

(20) Figueroa, A. I.; Harrison, S. E.; Collins-McIntyre, L. J.; van der Laan, G.; Hesjedal, T. Magnetic Ordering in Ho-Doped Bi 2 Te 3 Topological Insulator. *Phys. Status Solidi Rapid Res. Lett.* **2016**, *10*, 467−470.

(21) Harrison, S. E.; Collins-McIntyre, L. J.; Zhang, S. L.; Baker, A. A.; Figueroa, A. I.; Kellock, A. J.; Pushp, A.; Chen, Y. L.; Parkin, S. S. P.; Harris, J. S.; van der Laan, G.; Hesjedal, T. Study of Ho-Doped Bi2Te3 Topological Insulator Thin Films. *Appl. Phys. Lett.* **2015**, *107*, 182406.

(22) Díaz, B.; Rappl, P. H. O.; Abramof, E. Molecular Beam Epitaxial Growth of EuTe/SnTe Strained Superlattices. *J. Cryst. Growth* **2007**, *308*, 218−222.

(23) Caha, O.; Dubroka, A.; Humlíček, J.; Holý, V.; Steiner, H.; Ul-Hassan, M.; Sánchez-Barriga, J.; Rader, O.; Stanislavchuk, T. N.; Sirenko, A. A.; Bauer, G.; Springholz, G. Growth, Structure, and Electronic Properties of Epitaxial Bismuth Telluride Topological Insulator Films on BaF2 (111) Substrates. *Cryst. Growth Des.* **2013**, *13*, 3365−3373.

(24) Koma, A. New Epitaxial Growth Method for Modulated Structures Using Van Der Waals Interactions. *Surf. Sci.* **1992**, *267*, 29−33.

(25) Morelhão, S. L.; Kycia, S.; Netzke, S.; Fornari, C. I.; Rappl, P. H. O.; Abramof, E. Hybrid Reflections from Multiple X-Ray Scattering in Epitaxial Bismuth Telluride Topological Insulator Films. *Appl. Phys. Lett.* **2018**, *112*, 101903.

(26) Fornari, C. I.; Rappl, P. H. O.; Morelhão, S. L.; Abramof, E. Structural Properties of Bi2Te3 Topological Insulator Thin Films Grown by Molecular Beam Epitaxy on (111) BaF2 Substrates. *J. Appl. Phys.* **2016**, *119*, 165303.

(27) Fornari, C. I.; Rappl, P. H. O.; Morelhão, S. L.; Fornari, G.; Travelho, J. S.; de Castro, S.; Pirralho, M. J. P.; Pena, F. S.; Peres, M. L.; Abramof, E. Structural Defects and Electronic Phase Diagram of Topological Insulator Bismuth Telluride Epitaxial Films. *Mater. Res. Express* **2018**, *5*, 116410.

(28) Fornari, C. I.; Rappl, P. H. O.; Morelhão, S. L.; Peixoto, T. R. F.; Bentmann, H.; Reinert, F.; Abramof, E. Preservation of Pristine Bi 2 Te 3 Thin Film Topological Insulator Surface after Ex Situ Mechanical Removal of Te Capping Layer. *APL Mater.* **2016**, *4*, 106107.

(29) Morelhão, S. L.; Fornari, C. I.; Rappl, P. H. O.; Abramof, E. Nanoscale Characterization of Bismuth Telluride Epitaxial Layers by Advanced X-Ray Analysis. *J. Appl. Crystallogr.* **2017**, *50*, 399−410.

(30) Thole, B. T.; van der Laan, G.; Fuggle, J. C.; Sawatzky, G. A.; Karnatak, R. C.; Esteva, J.-M. 3d X-Ray-Absorption Lines and the 3 d 9 4 f n + 1 Multiplets of the Lanthanides. *Phys. Rev. B: Condens. Matter Mater. Phys.* **1985**, *32*, 5107−5118.

(31) Haverkort, M. W.; Zwierzycki, M.; Andersen, O. K. Multiplet Ligand-Field Theory Using Wannier Orbitals. *Phys. Rev. B: Condens. Matter Mater. Phys.* **2012**, *85*, 165113.

(32) Oh, S.-J.; Doniach, S. Screening Effects in the Core-Level Spectra of Mixed-Valence Compounds. *Phys. Rev. B: Condens. Matter Mater. Phys.* **1982**, *26*, 2085−2094.

(33) Harrison, S. E.; Collins-McIntyre, L. J.; Zhang, S.-L.; Baker, A. A.; Figueroa, A. I.; Kellock, A. J.; Pushp, A.; Parkin, S. S. P.; Harris, J. S.; van der Laan, G.; Hesjedal, T. Study of Dy-Doped Bi 2 Te 3 : Thin Film Growth and Magnetic Properties. *J. Phys. Condens. Matter* **2015**, *27*, 245602.

(34) Morelhão, S. L. Computer Simulation Tools for X-Ray Analysis. *Graduate Texts in Physics*; Springer International Publishing: Cham, 2016. .

(35) Steiner, H.; Volobuev, V.; Caha, O.; Bauer, G.; Springholz, G.; Holý, V. Structure and Composition of Bismuth Telluride Topological Insulators Grown by Molecular Beam Epitaxy. *J. Appl. Crystallogr.* **2014**, *47*, 1889−1900.

(36) Shannon, R. D. Revised Effective Ionic Radii and Systematic Studies of Interatomic Distances in Halides and Chalcogenides. *Acta Crystallogr. Sect. A* **1976**, *32*, 751−767.

(37) Tarakina, N. V.; Schreyeck, S.; Duchamp, M.; Karczewski, G.; Gould, C.; Brunner, K.; Molenkamp, L. W. Microstructural Characterization of Cr-Doped (Bi,Sb)2Te3 Thin Films. *CrystEngComm* **2017**, *19*, 3633−3639.

(38) Ghasemi, A.; Kepaptsoglou, D.; Galindo, P. L.; Ramasse, Q. M.; Hesjedal, T.; Lazarov, V. K. Van Der Waals Epitaxy between the Highly Lattice Mismatched Cu-Doped FeSe and Bi2Te3. *NPG Asia Mater* **2017**, *9*, No. e402.

(39) Hüfner, S. *Photoelectron Spectroscopy*, 2nd ed.; Cardona, M., Ed.; Springer-Verlag: Heidelberg, 1996.

(40) Balin, K.; Rapacz, R.; Weis, M.; Szade, J. Physicochemical Analysis of Bi2Te3 − (Fe, Eu) − Bi2Te3 Junctions Grown by Molecular Beam Epitaxy Method. *AIP Adv* **2017**, *7*, 056323.

(41) Kim, D.; Jin, Y.-H.; Jeon, K.-W.; Kim, S.; Kim, S.-J.; Han, O. H.; Seo, D.-K.; Park, J.-C. Blue-Silica by Eu 2+ -Activator Occupied in Interstitial Sites. *RSC Adv.* **2015**, *5*, 74790−74801.

(42) Ogasawara, H.; Kotani, A.; Thole, B. T. Lifetime Effect on the Multiplet Structure of 4 d X-Ray-Photoemission Spectra in Heavy Rare-Earth Elements. *Phys. Rev. B: Condens. Matter Mater. Phys.* **1994**, *50*, 12332−12341.

(43) Kinoshita, T.; Gunasekara, H. P. N. J.; Takata, Y.; Kimura, S.-i.; Okuno, M.; Haruyama, Y.; Kosugi, N.; Nath, K. G.; Wada, H.; Mitsuda, A.; Shiga, M.; Okuda, T.; Harasawa, A.; Ogasawara, H.; Kotani, A. Spectroscopy Studies of Temperature-Induced Valence Transition on EuNi 2 (Si 1- x Ge x) 2 around Eu 3 d −4 f , 4 d −4 f and Ni 2 p −3 d Excitation Regions. *J. Phys. Soc. Jpn.* **2002**, *71*, 148−155.

(44) Abdullayev, N. A.; Jafarli, K. M.; Aliguliyeva, K. V.; Aliyeva, L. N.; Kahramanov, S. S.; Nemov, S. A. Effect of Doping with Rare-Earth

https://dx.doi.org/10.1021/acs.jpcc.0c05077
J. Phys. Chem. C 2020, 124, 16048−16057

Elements (Eu, Tb, Dy) on the Conductivity of Bi2Te3 Layered Single Crystals. *Semiconductors* **2017**, *51*, 942−946.
(45) Massalski, T. B.; Murray, J. L.; Bennet, L. H. *Binary Alloy Phase Diagrams*; American Society for Metals, 1990; Vol. *1*.
(46) Zhang, L.; Zhao, D.; Zang, Y.; Yuan, Y.; Jiang, G.; Liao, M.; Zhang, D.; He, K.; Ma, X.; Xue, Q. Ferromagnetism in Vanadium-Doped Bi 2 Se 3 Topological Insulator Films. *APL Mater* **2017**, *5*, 076106.

https://dx.doi.org/10.1021/acs.jpcc.0c05077
J. Phys. Chem. C 2020, 124, 16048−16057